Laser safety for electro-optical imaging systems: exposure limits and hazard distances

Gunnar Ritt[ORCID],* Bastian Schwarz, Bernd Eberle, and Michael Henrichsen[ORCID]
Fraunhofer IOSB, Ettlingen, Germany

ABSTRACT. Laser safety with regard to the human eye is a well-known topic. Everybody working with laser sources has to follow the long-established occupational safety rules to prevent people from eye damage by accidental irradiation. These rules comprise, for example, the use of laser safety eyewear and the calculation of the maximum permissible exposure (MPE) and its corresponding hazard distance, the nominal ocular hazard distance. At exposure levels below the MPE, glare effects may occur if the laser wavelengths are in the visible spectral range. The physical effects of laser dazzling on the human eye are described by a quite new concept, which defines the maximum dazzle exposure (MDE) and the corresponding nominal ocular dazzle distance (NODD). Triggered by the MDE/NODD concept, we investigated whether similar laser safety calculations could be performed for electro-optical imaging systems. In this publication, we will review our approach for laser safety calculations for such systems. We have succeeded in finding closed-form equations, allowing calculations of exposure limits to prevent electro-optical imaging systems from damage and/or dazzle. Furthermore, we found some interesting effects related to the corresponding hazard distances, which are also discussed.

1 Introduction

Anyone who works professionally with lasers knows the long-established occupational safety rules to prevent eye damage by accidental laser irradiation. These include, among others, the calculation of the maximum permissible exposure (MPE) and its corresponding hazard distance, the nominal ocular hazard distance (NOHD)[1,2] as well as the choice of proper laser safety eyewear.[3,4] Quantities equivalent to MPE and NOHD but related to the reversible effect of laser eye dazzle were recently introduced by Williamson and McLin:[5–7] The maximum dazzle exposure (MDE) and nominal ocular dazzle distance (NODD). In the last years, we have attempted to define such quantities for electro-optical imaging systems and to derive equations to calculate those quantities, see Fig. 1. These are:

1. MPE for a sensor (MPE_S): the maximum applicable laser irradiance at the entrance aperture of the camera lens to prevent the image sensor from damage
2. nominal sensor hazard distance (NSeHD): the hazard distance corresponding to the MPE_S
3. MDE for a sensor (MDE_S): laser irradiance at the entrance aperture of the camera lens that corresponds to a certain dazzle level (see definition in Sec. 4.2)
4. nominal sensor dazzle distance (NSeDD): the hazard distance corresponding to the MDE_S.

---

*Address all correspondence to Gunnar Ritt, gunnar.ritt@iosb.fraunhofer.de
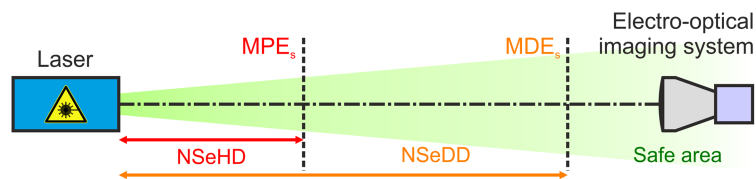
Fig. 1 ELs for electro-optical imaging systems (MPE_S and MDE_S) and corresponding hazard distances (NSeHD and NSeDD). Image reproduced with permission from Ref. 8.

In this publication, we review our work on laser safety calculations for electro-optical imaging systems, which was presented in detail in several journal articles and conference proceedings.[8–12] This includes the derivation of equations to estimate exposure limits (ELs; Sec. 4) and dazzle spot sizes (Sec. 5), approximations to estimate hazard distances (Sec. 6), suggestions for values of nonstandard parameters (Sec. 7), and the validation of this work by modeling and field trials (Sec. 8). We will not go into details here but mainly summarize the results of our work.

A brief note on terminology: We use the term *electro-optical imaging system* for a combination of a *camera lens* and a *camera*. The most important component of the camera for further discussion is the *image sensor*. Sometimes, we denote an electro-optical imaging system simply as a *sensor*.

2 Fundamentals

2.1 Objectives

When we started our work on this topic some years ago, we initially defined the objectives we wanted to reach. The main goal was to develop a tool for laser safety calculations for electro-optical imaging systems that can be applied also by users, who are not experts in this field, even though this may be associated with some limitation of accuracy. The objectives defined were:

Objective 1. Equivalent to laser safety calculations for the human eye, the values of MPE_S and MDE_S shall be related to the position of the entrance aperture of the camera lens.

Objective 2. All equations to calculate the laser safety quantities shall be given as closed-form expressions containing only commonly known operations and functions.

Objective 3. All equations to calculate the laser safety quantities should contain, as far as practical, only standard parameters of the involved devices (laser, camera lens, image sensor/camera) and the underlying scenario (e.g., distance, atmospheric extinction).

The formulated objectives have the following background: Objective 1 allows the user to position a power meter at the typically easily accessible place in front of the camera lens to compare calculated ELs with the incident laser irradiance. Objective 2 ensures that users who do not have relevant experience in this field can still perform laser safety calculations for sensors. In principle, everybody should be able to perform laser safety calculations using a sheet of paper and a pocket calculator. Therefore, we want to avoid numerical calculations that can only be performed with the help of a computer. Finally, Objective 3 shall enable the user to perform such calculations for a wide range of electro-optical imaging systems, i.e., for different combinations of camera lenses and image sensors, without the necessity to measure unknown parameters beforehand.

2.2 Approach

To derive damage-related laser safety quantities for electro-optical imaging systems analogous to those of the human eye (EL MPE and hazard distance NOHD), we had to start from the laser-induced damage threshold (LIDT) of the image sensor, which is located at the focal plane of the camera lens. Such damage thresholds for imaging sensors are usually not known and have to be determined by appropriate measurements, e.g., see the work of Becker et al.,[13,14] Théberge et al.,[15] Burgess et al.,[16] Westgate and James,[17] and Schwarz et al.[18–20] In the next step, we had to transfer the image sensor's damage threshold to the corresponding value at the position of the camera lens' entrance aperture to achieve Objective 1. However, this required finding out how the irradiance distribution of the threatening laser beam is related to the irradiance distribution in the

focal plane of the camera lens. This issue was the biggest step in our efforts to define the laser safety quantities for sensors since there is not, as with the human eye, only one single kind of camera lens but many different ones. The irradiance distribution at the focal plane depends on the design and quality of the camera lens, comprising its scattering characteristics and image distortions. The scattering properties of camera lenses are usually only very rarely known and must otherwise be determined in time-consuming measurements with a dedicated setup; see, e.g., Ref. 10.

The same considerations are also valid for dazzle-related laser safety quantities. For example, the laser dazzle threshold can be defined as the irradiance, where the pixels of the imaging sensor start to saturate. Such saturation thresholds can be calculated easily from the specifications of the image sensor.[9] However, to describe the extent of laser dazzle, i.e., the size of the dazzle spot on the image sensor, we again need the quantitative irradiance distribution at the focal plane to compare it with the saturation threshold.

In summary: the basis for achieving our goal was to set up a theoretical model (based on closed-form equations to achieve Objective 2) that quantitatively describes the irradiance distribution at the focal plane of a camera lens in the case of laser irradiation. For our application, the main focus of the theoretical model was that it is capable of describing the irradiance distribution in an appropriate manner for our laser safety calculations. There was no intent that the theoretical model describes the irradiance distribution perfectly accurate, so it may also be used for other purposes (e.g., stray light analysis in optics design).

Therefore, we concentrated on the estimation of the peak irradiance (which is crucial for laser damage) and the estimation of the large-scale irradiance distribution (which is crucial for the laser dazzle effect). This means that we included diffraction effects in the theoretical model regarding the peak irradiance and scatter/stray light effects for the large-scale irradiance distribution. The importance of including stray light for the calculation of the focal plane irradiance distribution was shown, for example, by Benoist and Schleijpen,[21] who modeled the size of laser dazzle spots for charge-coupled device (CCD) cameras.

However, we did not include aberrations in our theoretical model since aberrations have typically only an influence on the spatial irradiance distribution near the center of the laser spot at the image sensor as long as the imaging system is focused. The inclusion of aberrations is only required for an accurate description of very small laser dazzle spots in the order of some pixels in diameter, which is rather irrelevant for practical use. Regarding laser dazzle, our interest laid on the description of dazzle spots that affect a considerable amount of the sensor's field of view (FOV; >10%). Also, specific optical effects, such as diffraction spikes, have not been considered since they have an influence on the sensor image only in very limited areas and thus have little impact on the overall perceptibility of the scene.

2.3 Scenario

For our laser safety calculations, we assumed the scenario shown in Fig. 2. A laser emits a Gaussian beam characterized by the output power, P_0; the laser wavelength, λ; the output beam
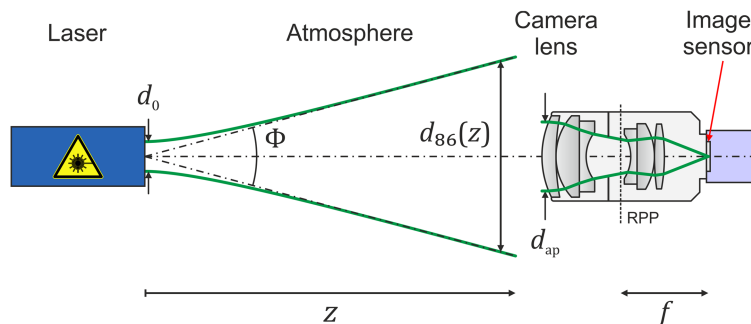
Fig. 2 Schematic view of a dazzle scenario. RPP, rear principal plane. Please note that the location and size of the apertures and pupils are drawn for illustrative purposes only. Image reproduced with permission from Ref. 8.

diameter, d_0; and the full angle divergence, Φ. The laser radiation illuminates an electro-optical imaging system consisting of a camera lens and a camera with an image sensor. The laser beam diameter at the camera lens is denoted by d_{86}, which refers (in the case of Gaussian beams) to the two opposing positions at the radial irradiance profile, where the irradiance dropped to $1/e^2$ of the peak irradiance.

The camera lens is described by the focal length f and the diameter of the entrance pupil d_{ap}. We would like to point out that the location and size of the entrance pupil and the rear principle plane as well as the beam paths in Fig. 2 are drawn for illustrative purposes only. Further parameters of the camera lens are the f-number $F = f/d_{ap}$, the number of optical elements N_{oe}, the transmittance T, and three scatter parameters s, b_0 (or alternatively b), and l, which will be described in more detail in Sec. 3.1.

The ratio of the beam diameter d_{86} to the diameter of the camera lens' entrance pupil d_{ap} is called the truncation factor ν and, as we will see later, has a determining influence on the distribution of the laser light in the focal plane of the camera lens

$$\nu = d_{86}/d_{ap}, \tag{1}$$

where the laser beam diameter d_{86} in a distance z to the laser source can be calculated by

$$d_{86}(z) = \sqrt{d_0^2 + \Phi^2 z^2}. \tag{2}$$

Using the truncation factor ν, the fraction P_{in} of the laser power P_0 that enters the lens can be calculated by

$$P_{in} = P_0 \left(1 - \exp\left(-\frac{2}{\nu^2} \right) \right). \tag{3}$$

The image sensor is characterized by several parameters: the number of pixel columns and rows N_{col}, N_{row}, pixel size p, total quantum efficiency η, saturation capacity C, and the integration time t_{exp}. We assume that the sensor system is well focused, i.e., the imaging sensor is placed at (or very near to) the focal plane of the camera lens. The onset of damage and dazzle is described by irradiance values E_{dam} (LIDT) and E_{sat} (saturation irradiance).

The attenuation of laser power by the atmosphere may be included by substituting P_0 with $P_0 \cdot \exp(-\mu z)$, where μ is the atmospheric extinction coefficient.

2.4 Parameters

Table 1 summarizes all parameters that we use for our laser safety calculations.

According to Objective 3, our equations shall be based only on standard parameters that are typically specified by the manufacturers of lasers, camera lenses, or image sensors. However, besides such standard parameters, some of the aforementioned parameters are usually not specified or known:

1. the LIDT of the image sensor E_{dam}
2. the saturation irradiance of the image sensor E_{sat} and
3. the scatter parameters of the camera lens: s, b_0, l.

In Sec. 7, we state values/equations for these nonstandard parameters that may be used, if measured values for a specific electro-optical imaging system are not available.

3 Estimation of the Focal Plane Irradiance Distribution

In our theoretical model, the incident power P_{in} contributes to the focal plane irradiance distribution E_{fp} by two components: (a) the scatter/stray light component E_s and (b) the diffraction component E_d:

$$E_{fp}(r) = E_s(r) + \eta_d E_d(r), \tag{4}$$

where η_d describes the fraction of the incident laser power that is diffracted and r is the radial coordinate. In Eq. (4), as well as in all subsequent equations, the dependency on the radial

Table 1 Parameters used for the laser safety calculations.

Symbol	Unit	Quantity
Laser		
P_0	W	Power
d_{86}	m	Beam diameter at the camera lens ($1/e^2$)
d_0	m	Beam diameter at the laser output
Φ	rad	Beam divergence
λ	m	Wavelength
Camera lens		
f	m	Focal length
d_{ap}	m	Aperture/entrance pupil diameter
$F = f/d_{ap}$		f-Number
N_{oe}		Number of optical elements
$N_{ss} = 2 \cdot N_{oe}$		Number of scattering surfaces
T		Transmittance
s; b_0; b; l	—; sr^{-1}; sr^{-1}; rad	Scatter parameters
Image sensor/camera		
p	m	Pixel size
A	m^2	Pixel area
C	e$^-$	Saturation capacity
η		Total quantum efficiency
t_{exp}	s	Exposure time
E_{sat}	W/m^2	Saturation threshold
E_{dam}	W/m^2	LIDT
N_{col}; N_{row}		No. of pixels per column and row
Miscellaneous		
r	m	Radial coordinate
$\nu = d_{86}/d_{ap}$		Truncation factor
$P_{in} = P_0(1 - \exp(-2/\nu^2))$	W	Laser power entering the camera lens
$d_{spot} = k\lambda F$	m	Laser spot size in the focal plane
K		Spot size constant

coordinate r (in the focal plane) can be replaced by the dependency on the viewing angle Θ using the relationship

$$\Theta = \frac{r}{f} \Leftrightarrow r = \Theta f. \tag{5}$$

3.1 Stray Light Component

To estimate the contribution of the stray light E_s to the focal plane irradiance distribution E_{fp}, we relied on the work of Peterson,[22] who published an analytical approach for this task using the three-parameter Harvey scatter model as a bidirectional scattering distribution function (BSDF).

This type of BSDF describes the angular distribution of stray light caused by scatter from smooth surfaces of optical elements using three parameters, s, b_0, and l. Other sources of stray light such as multiple reflections or scatter from the lens housing are not considered. For a detailed explanation of the BSDF and the meaning of the scatter parameters, we refer the reader to other publications, e.g., Ref. 23.

For our theoretical model, we applied some simplifications (see Ref. 9 for more details) to the work of Peterson[22] to keep equations manageable for typical camera lenses with five or more optical elements. As a result, we calculate the stray light component by

$$E_{\rm s}(r) = \frac{P_0 T N_{\rm ss} b_0}{f^2 (v^*)^2} \left[1 + \left(\frac{r}{v^* l f} \right)^2 \right]^{\frac{s}{2}} \cdot \left(1 - \exp\left(-\frac{2}{v^2} \right) \right), \tag{6}$$

where v^* is defined by

$$\nu^* = \min\left(1, \frac{\nu}{\sqrt{2}} \right). \tag{7}$$

$N_{\rm ss}$ is the number of scattering surfaces of the camera lens, which we assume is twice the number of optical elements $N_{\rm oe}$. The modified truncation factor ν^* considers that the beam diameter within the camera lens cannot increase, if a laser beam, which is already much larger than the entrance aperture, would expand further, e.g., with increasing distance to the laser source.

The ratio of scattered power to the incident power (for a single scattering surface) is called the total integrated scatter (TIS) and can be calculated by[23]

$$\text{TIS} = \begin{cases} 2\pi b \frac{100^s}{s+2} \left[(1 + l^2)^{\frac{s+2}{2}} - (l^2)^{\frac{s+2}{2}} \right], & s \neq -2 \\ 2\pi b \frac{(100 l)^s}{2} l^2 \ \ln\left(1 + \frac{1}{l^2} \right), & s = -2 \end{cases} . \tag{8}$$

Please note: Eq. (8) uses an alternative scatter parameter b that has its origins in the *two*-parameter Harvey scatter model (see, e.g., Ref. 21). This scatter parameter b is linked to scatter parameter b_0 by the following equation:

$$b_0 = b \cdot (100 l)^s. \tag{9}$$

The quantity TIS is used to calculate the fraction $\eta_{\rm d}$ of the incident power that is diffracted; see Eq. (4)

$$\eta_{\rm d} = (1 - TIS)^{N_{\rm ss}}. \tag{10}$$

The scatter parameters are wavelength dependent; the wavelength dependency is described by the equation[24]

$$b(\lambda) = b(\lambda_0) \left(\frac{\lambda_0}{\lambda} \right)^{4+s} \quad s(\lambda) = s(\lambda_0) \quad l(\lambda) = l(\lambda_0) \left(\frac{\lambda}{\lambda_0} \right). \tag{11}$$

Reference 24 stated that these wavelength scaling laws are valid only "over a limited range of λ," but limits are not given. Wein,[25] for example, stated that the "wavelength scaling approximately predicts the scattering in the visible but not in the far infrared."

3.2 Diffraction Component
For the diffraction component $E_{\rm d}$, we assumed in our theoretical model a Gaussian beam and used for our calculations the work of Urey[26] regarding the diffraction pattern of a truncated Gaussian beam. This diffraction pattern can be imagined to look like something between the Airy diffraction pattern and a pure Gaussian distribution. The shape depends on the value of the truncation factor ν and consists of a central lobe that can be approximated by a Gaussian distribution and diffraction rings of lower power similar to the Airy diffraction pattern.

The central lobe is approximated by

$$E_{\rm cl}(r) = E_0(\nu) \ \exp\left(-8 \frac{r^2}{d_{\rm spot}^2} \right), \tag{12}$$

where the peak irradiance of the diffraction pattern is given by

$$E_0(\nu) = \frac{P_0 T \pi}{4 \lambda^2 F^2} \cdot 2\nu^2 \left[1 - \exp\left(-\frac{1}{\nu^2}\right) \right]^2, \tag{13}$$

and the spatial extent of the central lobe is calculated by[26]

$$d_{\text{spot}} = K \lambda F. \tag{14}$$

Here, K is a spot size constant, which also depends on the truncation factor ν, see Ref. [26] for details

$$K = \frac{0.97}{\nu} \sqrt{\frac{\exp(1)}{1 - \exp\left(-\frac{1}{\nu^2}\right)} - 1}. \tag{15}$$

For a typical camera lens designed for the visible spectral range, the diffraction spot size d_{spot} is usually in the order of some micrometers. Since the pixel size of common CCD or complementary metal-oxide-semiconductor (CMOS) image sensors is of the same order, the central lobe is usually not resolved by an image sensor. Thus, for our laser safety calculations, we relied on the peak irradiance $E_0(\nu)$ only.

Outside the central lobe, the wings of the diffraction pattern are described by the mean of the diffraction ring irradiance, which is given by

$$E_{\text{dr}}(r) = \frac{P_0 T \lambda F}{\pi^3 r^3} \cdot \frac{2}{\nu^2} \exp\left(-\frac{2}{\nu^2}\right). \tag{16}$$

Since Eq. (16) describes the mean of the diffraction ring irradiance, there is no oscillating term in the formula. Here, the diffraction ring irradiance E_{dr} is a monotonically decreasing function with a $1/r^3$ dependence.

3.3 Focal Plane Irradiance Distribution

Some examples of radial irradiance profiles as calculated with Eq. (4) are plotted in Fig. 3. The three graphs show the normalized irradiance as a function of the radial coordinate r for different values of the truncation factor ν. For the calculations, the parameters listed in Table 2 were used.

4 Exposure Limits

After setting up the theoretical model for the focal plane irradiance distribution, the EL MPE_S and MDE_S could be derived. For the derivation of these two quantities, we did not employ the exact equation for $E_{\text{fp}}(r)$ but used only the respective essential components. This means that we used the peak irradiance $E_0(r)$ only for the derivation of the MPE_S since the onset of laser damage depends on the peak irradiance. By contrast, the derivation of the MDE_S is based on the irradiance of the diffraction rings $E_{\text{dr}}(r)$ and the stray light irradiance E_s since the spatial extent of the dazzle spot essentially depends only on these components; see Fig. 3. Only for the treatment of tiny dazzle spots, the irradiance of the central lobe $E_{\text{cl}}(r)$ would be needed. As mentioned before, we considered this case as not relevant for practical use and focused on larger dazzle spots that comprise considerable amounts of the sensors FOV (>10%).

4.1 MPE for a Sensor

The MPE_S can be calculated by equalizing the focal plane peak irradiance $E_0(\nu)$ of Eq. (13) and the image sensor's damage threshold E_{dam}. This leads to

$$E_0(\nu) = \frac{P_{\text{max}} T \pi}{4 \lambda^2 F^2} \cdot 2\nu^2 \left[1 - \exp\left(-\frac{1}{\nu^2}\right) \right]^2 \stackrel{\text{def}}{=} E_{\text{dam}}. \tag{17}$$

Resolving for the maximum permissible laser power P_{max} and calculating the corresponding laser peak irradiance by dividing P_{max} by $\frac{\pi}{8} d_{86}^2 = \frac{\pi}{8} (\nu \frac{f}{F})^2$ result in the searched quantity MPE_S

Theoretical focal plane irradiance profiles
for different values of truncation factor ν
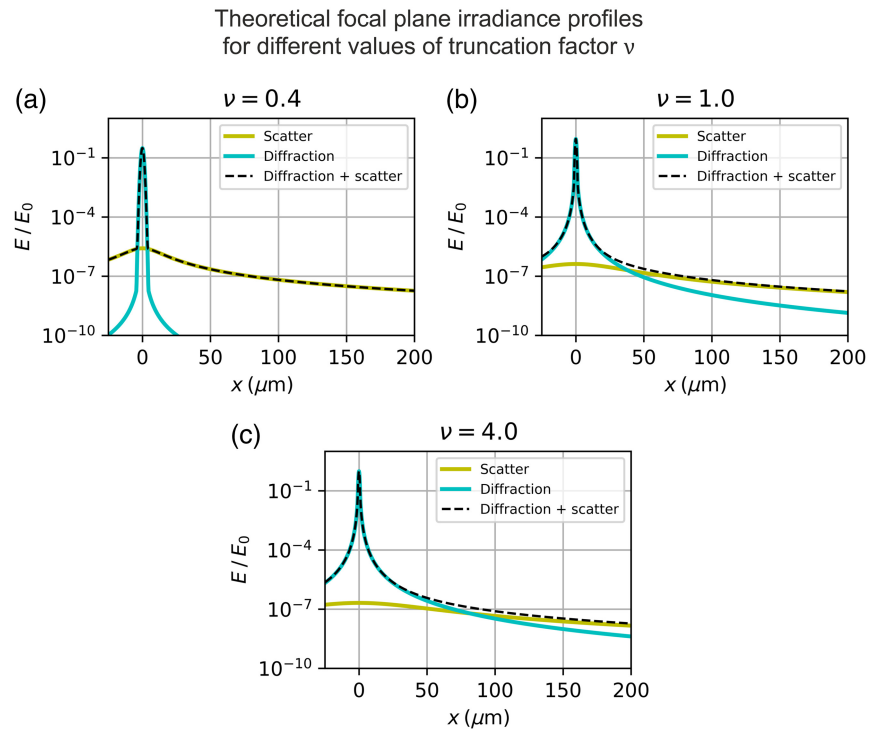
Fig. 3 Example of (normalized) focal plane irradiance profiles according to Eq. (4) for a specific set of parameters and three values of truncation factor: (a) $\nu = 0.4$, (b) $\nu = 1.0$, and (c) $\nu = 4.0$.

Table 2 Parameters used for the example calculations of Figs. 3 and 5.

Laser	
Wavelength λ	532 nm
Output power P_0	5 mW
Output diameter ($1/e^2$) d_0	3.5 mm
Full angle divergence ($1/e^2$) Φ	0.5 mrad
Camera lens	
Focal length f	25 mm
f-Number F	1.8
No. of optical elements N_{oe}	7
Transmittance T	0.89
Scatter parameter (@ 550 nm) s	-1.86
Scatter parameter (@ 550 nm) b	0.36 sr^{-1}
Scatter parameter (@ 550 nm) b_0	6.92 sr^{-1}
Scatter parameter (@ 550 nm) l	2.04 mrad
Image sensor/camera	
Size ($N_{col} \times N_{row}$)	808 px. $\times$ 608 px.
Pixel size p	4.8 μm
Quantum efficiency η	0.53
Exposure time t_{exp}	20 ms
Saturation capacity C	7230 e$^-$
Damage threshold E_{dam}	73 kW/cm^2

$$\mathrm{MPE_S} = E_{\mathrm{dam}} \cdot \frac{16\lambda^2 F^4}{T\pi^2 f^2} \left[\frac{\frac{1}{\nu^2}}{1 - \exp\left(-\frac{1}{\nu^2}\right)} \right]^2. \tag{18}$$

From Eq. (18), we see that the $\mathrm{MPE_S}$ depends on the truncation factor, which means that the $\mathrm{MPE_S}$ also depends on the distance of the laser to the imaging system. This has a crucial impact on the calculation of the corresponding hazard distance, as we will explain in more detail in Sec. 6.

The lowest value of the $\mathrm{MPE_S}$ (worst case) occurs for $\nu \to \infty$

$$\mathrm{MPE_{S,min}} = \lim_{\nu \to \infty} \mathrm{MPE_S} = E_{\mathrm{dam}} \cdot \frac{16\lambda^2 F^4}{T\pi^2 f^2}. \tag{19}$$

Equation (19) is applicable when the laser source is far away from the electro-optical imaging system and the laser beam overfills the aperture of the camera lens. In this case, no distance dependence exists.

4.2 MDE for a Sensor

For the human eye, the MDE is not just a single value but is stated for specific dazzle levels.[6,7] The dazzle levels range from very low to low, medium, and high, which corresponds to angular dazzle fields of 2, 10, 20, and 40 deg, respectively. For electro-optical imaging systems, an equivalent definition of such default values for the dazzle field is not useful since the system's FOV changes with the focal length of the camera lens.

For an imaging system, we defined the dazzle level as the fraction ϵ of the system's FOV that is dazzled. This means, e.g., that for an incident irradiance of $\mathrm{MDE_S}(\epsilon = 0.1)$ $\mathrm{MDE_S}(\epsilon = 0.5)$, and $\mathrm{MDE_S}(\epsilon = 1.0)$, a tenth of the FOV, half of the FOV, and the full FOV are dazzled, respectively. Figure 4 illustrates that approach. The fraction ϵ shall be understood as the diameter of the dazzle spot divided by the size of the longer side of the image sensor.

Using this definition, the angular *radius* of the dazzle spot is

$$\Theta_\epsilon = \epsilon \cdot \frac{\mathrm{FOV}}{2}, \tag{20}$$

where the FOV of the imaging system can be calculated by

$$\mathrm{FOV} = \frac{N_{\max} \cdot p}{f} \quad \text{with } N_{\max} = \max(N_{\mathrm{col}}, N_{\mathrm{row}}). \tag{21}$$

We can find the $\mathrm{MDE_S}$ for a specific dazzle level ϵ by equating the focal plane irradiance distribution $E_{\mathrm{fp}}(\Theta_\epsilon)$ and the image sensor's saturation threshold E_{sat}. As previously addressed, we approximate the focal plane irradiance distribution $E_{\mathrm{fp}}(\Theta_\epsilon)$ for this case through the diffraction ring irradiance $E_{\mathrm{dr}}(r)$ and the stray light component $E_{\mathrm{s}}(r)$. Thus, we obtain the following equation:

$$E_{\mathrm{fp}}(r = \Theta_\epsilon f) \approx E_{\mathrm{dr}}(\Theta_\epsilon f) + E_{\mathrm{s}}(\Theta_\epsilon f) \overset{\mathrm{def}}{=} E_{\mathrm{sat}} \Leftrightarrow, \tag{22}$$
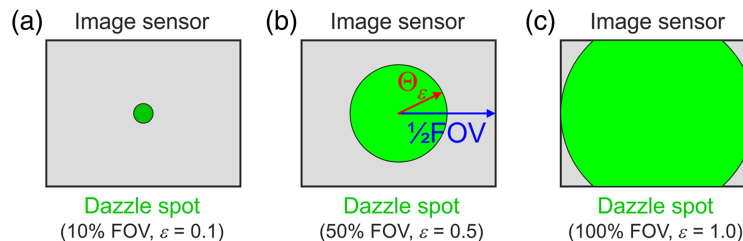
Fig. 4 Definition of dazzle levels as the fraction of the imaging system's FOV that is dazzled: (a) dazzle level $\epsilon = 0.1$, (b) dazzle level $\epsilon = 0.5$, and (c) dazzle level $\epsilon = 1.0$. Image reproduced with permission from Ref. 9.

$$\frac{P_{\max}T\lambda F}{\pi^3\Theta_\epsilon^3 f^3}\cdot\frac{2}{\nu^2}\,\exp\left(-\frac{2}{\nu^2}\right)+\frac{P_{\max}TN_{\mathrm{ss}}b_0}{f^2(v^*)^2}\left[1+\left(\frac{\Theta_\epsilon}{v^*l}\right)^2\right]^{\frac{s}{2}}\cdot\left(1-\exp\left(-\frac{2}{\nu^2}\right)\right)\overset{\mathrm{def}}{=}E_{\mathrm{sat}}. \quad (23)$$

Equivalent to the $\mathrm{MPE_S}$, the searched quantity $\mathrm{MDE_S}$ can be derived by resolving for the maximum permissible laser power $P_{\max}$ and calculating the corresponding laser irradiance by dividing $P_{\max}$ by $\frac{\pi}{8}d_{86}^2=\frac{\pi}{8}\left(\nu\frac{f}{F}\right)^2$

$$\mathrm{MDE_S}(\epsilon)=\frac{4E_{\mathrm{sat}}F^2}{\pi T}\frac{1}{\frac{\lambda F}{\pi^3 f\Theta_\epsilon^3}\cdot\exp\left(-\frac{2}{\nu^2}\right)+\frac{N_{\mathrm{ss}}b_0}{(v^*)^2}\left[1+\left(\frac{\Theta_\epsilon}{v^*l}\right)^2\right]^{\frac{s}{2}}\cdot\frac{\left(1-\exp\left(-\frac{2}{\nu^2}\right)\right)}{2/\nu^2}}. \quad (24)$$

As in the case of the $\mathrm{MPE_S}$, the equation simplifies for the case of $\nu\to\infty$, which gives the minimum value of the $\mathrm{MDE_S}$

$$\mathrm{MDE_{S,min}}(\epsilon)=\lim_{\nu\to\infty}\mathrm{MDE_S}(\epsilon)=\frac{4E_{\mathrm{sat}}F^2}{\pi T}\frac{1}{\frac{\lambda F}{\pi^3 f\Theta_\epsilon^3}+N_{\mathrm{ss}}b_0\left[1+\left(\frac{\Theta_\epsilon}{l}\right)^2\right]^{\frac{s}{2}}}. \quad (25)$$

Equations (24) and (25) should not be used for vanishing values of ϵ, such as $\epsilon=0$ or ϵ very close to zero, see Ref. 9 for more details. The value $\mathrm{MDE_S}(\epsilon=0)$ would correspond to the onset of laser dazzle. This onset can be estimated using Eq. (18) or (19) but replacing the focal plane damage threshold E_{dam} by the saturation threshold E_{sat}

$$\mathrm{MDE_S}(\epsilon=0)=E_{\mathrm{sat}}\cdot\frac{16\lambda^2 F^4}{T\pi^2 f^2}\left[\frac{\frac{1}{\nu^2}}{1-\exp\left(-\frac{1}{\nu^2}\right)}\right]^2, \quad (26)$$

$$\mathrm{MDE_{S,min}}(\epsilon=0)=\lim_{\nu\to\infty}\mathrm{MDE_S}(\epsilon=0)=E_{\mathrm{sat}}\cdot\frac{16\lambda^2 F^4}{T\pi^2 f^2}. \quad (27)$$

5 Dazzle Spot Size

The size of a dazzle spot Θ_{ds} can be calculated by solving Eq. (22) for Θ

$$E_{\mathrm{fp}}(\Theta_{\mathrm{ds}})\approx E_{\mathrm{dr}}(\Theta_{\mathrm{ds}})+E_{\mathrm{s}}(\Theta_{\mathrm{ds}})=E_{\mathrm{sat}}. \quad (28)$$

Unfortunately, there is no closed-form expression for this solution. This equation can be solved numerically using a computer. However, an approximate analytic solution can be given by solving the equations for the diffracted irradiance and the scattered irradiance individually and choosing the maximum value as the dazzle radius.

The equation to solve for the irradiance of the diffraction rings E_{dr} is

$$E_{\mathrm{dr}}(\Theta_{\mathrm{ds,d}})=\frac{P_0 T\lambda F}{\pi^3 f^3}\frac{1}{\Theta_{\mathrm{ds,d}}^3}\cdot\frac{2}{\nu^2}\,\exp\left(-\frac{2}{\nu^2}\right)=E_{\mathrm{sat}}, \quad (29)$$

and the equation to solve for the scattered irradiance E_s is

$$E_{\mathrm{s}}(\Theta_{\mathrm{ds,s}})=\frac{P_0 TN_{\mathrm{ss}}b_0}{f^2}\frac{1}{(v^*)^2}\left[1+\frac{1}{(v^*)^2}\left(\frac{\Theta_{\mathrm{ds,s}}}{l}\right)^2\right]^{\frac{s}{2}}\cdot\left(1-\exp\left(-\frac{2}{\nu^2}\right)\right)=E_{\mathrm{sat}}. \quad (30)$$

Solving Eqs. (29) and (30) for $\Theta_{\mathrm{ds,d}}$ and, $\Theta_{\mathrm{ds,s}}$ respectively, we obtain

$$\Theta_{\mathrm{ds,d}}=\sqrt[3]{\frac{P_0 T}{E_{\mathrm{sat}}}\cdot\frac{\lambda F}{\pi^3 f^3}\cdot\frac{2}{\nu^2}\,\exp\left(-\frac{2}{\nu^2}\right)}, \quad (31)$$

$$\Theta_{\mathrm{ds,s}}=v^*l\cdot\sqrt{\left(\frac{E_{\mathrm{sat}}}{P_0 T}\cdot\frac{f^2(v^*)^2}{N_{\mathrm{ss}}b_0}\cdot\frac{1}{\left(1-\exp\left(-\frac{2}{\nu^2}\right)\right)}\right)^{\frac{2}{s}}-1}, \quad (32)$$

and finally

$$\Theta_{ds} \approx \max(\Theta_{ds,d}, \Theta_{ds,s}). \tag{33}$$

6 Hazard Distances

Unfortunately, the calculation of hazard distances for electro-optical imaging systems is different compared with those for the human eye. As we can see from Eqs. (18) and (24), both the MPE_S and the MDE_S depend on the truncation factor ν. This implicates a dependence of these ELs on the distance between the laser source and imaging system since the beam diameter changes with distance and thus the truncation factor does. The conventional equations to calculate the human eye-related NOHD and NODD (neglecting atmospheric extinction) are

$$NOHD = \frac{\sqrt{\frac{4P_0}{\pi \cdot MPE} - d_0^2}}{\Phi}, \tag{34}$$

$$NODD = \frac{\sqrt{\frac{4P_0}{\pi \cdot MDE} - d_0^2}}{\Phi}. \tag{35}$$

Please note that the beam diameter d_0 and divergence Φ in Eqs. (34) and (35) have to refer to the opposite positions of the laser beam profile at which the irradiance has dropped to $1/e$ of the peak irradiance. This is a common practice in laser safety, whereas, in this publication, we typically refer to the $1/e^2$ points unless otherwise stated.

Nevertheless, these equations cannot be applied in our case, even if the correct quantities are used since Eqs. (34) and (35) were derived for distance-independent ELs. The distance-dependent values of MPE_S and MDE_S are plotted in Fig. 5 for a generic electro-optical imaging system and laser source; the parameters assumed for this calculation are listed in Table 2.

For the graph in Fig. 5(a), the independent parameter is the distance z of the electro-optical imaging system to the laser source, whereas, for the graph in Fig. 5(b), we used the truncation factor $\nu = d_{86}/d_{ap} = \sqrt{d_0^2 + \Phi^2 z^2}/d_{ap}$ as the independent parameter. While the MPE_S is a single curve (plotted in red), the MDE_S is represented by a light blue band, which indicates the range of MDE_S values for various dazzle levels $\epsilon \in [0.1; 1.0]$. The MDE_S curve for $\epsilon = 0.5$ is highlighted by a blue line; the upper and lower border of the blue band correspond to $\epsilon = 1.0$ and $\epsilon = 0.1$, respectively. In addition, the laser peak irradiance at the front face of the camera lens is shown as a green curve. Please note that the parameter E_{dam} in Table 2 is related to the focal plane, whereas the ordinate of the plot is related to the front face of the camera lens.

In Fig. 5, we can recognize how the MPE_S and MDE_S vary with distance. Following the curves starting from large distance values, the ELs are quite constant, which correspond to the minimum values as given by Eqs. (19) and (25). For closer distances from ~40 to ~4 m, the ELs
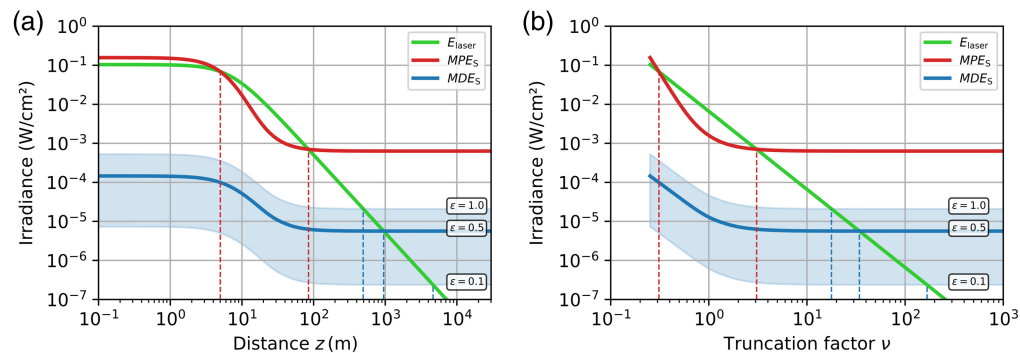
Fig. 5 Example of MPE_S (red line) and MDE_S (light blue band corresponding to various values of dazzle level ϵ) for an arbitrarily chosen scenario as the function of the distance between the imaging system and laser source. In addition, the peak irradiance of the assumed laser source at the position of the lens is shown (green line). The parameters used for the calculations are listed in Table 2. Independent parameter: (a) distance z and (b) truncation factor ν. Graphs reproduced with permission from Ref. 8.

increase strongly (for the given example) with decreasing distance. Finally, for distances below ~1 m, the ELs stay constant again.

A very important result concerns the hazard distance regarding the $\mathrm{MPE_S}$ curve: Looking at the green curve, which indicates the laser peak irradiance, we can see that this curve intersects the $\mathrm{MPE_S}$ curve twice. As long as the irradiance curve is below the $\mathrm{MPE_S}$ curve, the imaging system is safe from damage. In the distance range where the irradiance curve is above the $\mathrm{MPE_S}$ curve, the imaging system is not safe from damage. By the example of Fig. 5, we can recognize two intersection points ν_{hd}, which cut the $\mathrm{MPE_S}$ curve into three sections (see vertical dashed red lines): In the first section, the image sensor is safe from damage within the distance from the laser to the first intersection point. Between the two intersection points, the image sensor is not safe from damage, and in section three, beyond the second intersection point, the image sensor is again safe from damage. This means that the laser hazard zone for imaging systems may have a distance dependent upper as well as a lower limit. This is in contrast to laser hazard distances valid for the human eye.

We acknowledge that we intentionally chose the laser parameters in such a way that this effect is eye-catching in the example of Fig. 5. If we choose a sufficiently higher value of laser power P_0, the irradiance curve would be shifted so much upward that the irradiance curve would intersect the $\mathrm{MPE_S}$ curve only once. In our example, this is the case for the $\mathrm{MDE_S}$ curves in Fig. 5. For each dazzle level ϵ (0.1, 0.5, or 1.0), the irradiance curve will intersect a specific $\mathrm{MDE_S}$ curve only once. For another choice of system parameters (mainly the scatter parameter s) that may be different.

6.1 Derivation of Hazard Distances

The hazard distances NSeHD and NSeDD are defined by the fact that the laser irradiance at the system's camera lens E_{laser} is equal to the $\mathrm{MPE_S}$ and $\mathrm{MDE_S}$, respectively. Using EL as a synonym for either the $\mathrm{MPE_S}$ or the $\mathrm{MDE_S}$, this means that

$$E_{\mathrm{laser}}(z_{\mathrm{hd}}) = \frac{8P_0}{\pi d_{86}^2(z_{\mathrm{hd}})} \overset{\mathrm{def}}{=} \mathrm{EL}, \tag{36}$$

with

$$d_{86}(z_{\mathrm{hd}}) = \sqrt{d_0^2 + \phi^2 z_{\mathrm{hd}}^2} = \nu_{\mathrm{hd}} \cdot d_{\mathrm{ap}} = \nu_{\mathrm{hd}} \cdot \frac{f}{F}, \tag{37}$$

where ν_{hd} is the truncation factor in the hazard distance z_{hd}. Resolving Eq. (36) for z_{hd} would result in the hazard distance NSeHD/NSeDD. Unfortunately, there is no solution in closed form, when we apply Eqs. (18) and (24) for the $\mathrm{MPE_S}$ and the $\mathrm{MDE_S}$ in Eq. (36), respectively.

We recognized that the truncation factor ν is the determining parameter for the $\mathrm{MPE_S}$ and $\mathrm{MDE_S}$. Thus, we chose in the first step the approach not to determine z_{hd} but the corresponding truncation factor ν_{hd}. This led to somewhat easier equations for the derivation of the NSeHD and the NSeDD, although these equations were still not resolvable analytically but only numerically.

Then, in a second step, the terms of the equations to be solved, which depended on the truncation factor ν, were substituted by approximations that allowed solutions for ν_{hd} in closed form. We refer the reader to Ref. 8 for detailed explanations and will present here the results only.

Finally, having an approximation for ν_{hd}, the corresponding hazard distance z_{hd} (NSeHD or NSeDD) can then be calculated by

$$z_{\mathrm{hd}} = \frac{\sqrt{\nu_{\mathrm{hd}}^2 \cdot f^2/F^2 - d_0^2}}{\Phi}. \tag{38}$$

6.2 Nominal Sensor Hazard Distance

For the NSeHD, we found approximate estimates both for the upper and lower values of ν_{hd}[8]

$$v_{uhd}^2 = \frac{K}{2} + \sqrt{\frac{K^2}{4} - 1} = \frac{P_0 T \pi}{4 E_{dam} \lambda^2 F^2} + \sqrt{\left(\frac{P_0 T \pi}{4 E_{dam} \lambda^2 F^2}\right)^2 - 1},$$

$$v_{lhd}^2 = \frac{K}{2} - \sqrt{\frac{K^2}{4} - 1} = \frac{P_0 T \pi}{4 E_{dam} \lambda^2 F^2} - \sqrt{\left(\frac{P_0 T \pi}{4 E_{dam} \lambda^2 F^2}\right)^2 - 1}, \quad (39)$$

which can be used to calculate the upper and lower values of the laser hazard zone by

$$\text{NSeHD} = \frac{\sqrt{\nu_{hd}^2 \cdot f^2/F^2 - d_0^2}}{\Phi} \quad \text{with } \nu_{hd} \in (\nu_{uhd}, \nu_{lhd}). \quad (40)$$

These approximations are well usable to determine hazard distances for sensor damage. In Ref. 8, approximate values of NSeHD calculated using Eqs. (39) and (40) (NSeHD_{appr}) were compared with values computed by numerically solving Eq. (36) (NSeHD_{num}). The calculations were performed for a total of 5734 different parameter sets. The relative error of the approximate NSeHD values

$$\delta\text{NSeHD} = (\text{NSeHD}_{appr} - \text{NSeHD}_{num})/\text{NSeHD}_{num}, \quad (41)$$

was between [0, +0.5] in more than 90% of cases. The results are graphically displayed in Fig. 6: Fig. 6(a) as a histogram of the δNSeHD values (bin width 0.5) and Fig. 6(b) a plot of the relative error δNSeHD as a function of the numerically calculated value of the truncation factor ν_{hd}. In both graphs, red and blue color correspond to the upper and lower values of the hazard distance, respectively.

We found an overestimation of values rather than an underestimation, which is good in terms of laser safety. However, it should be noted that these investigations were based on a limited database and the results may not be generally valid.

6.3 Nominal Sensor Dazzle Distance

The search for a closed-form expression to calculate the NSeDD was quite demanding. This is due to the fact that the equation that has to be solved to calculate the NSeDD is quite complex. As for the NSeHD, there may be an upper and lower limit of the laser hazard zone. Furthermore, for a specific dazzle level E, there may be areas within the laser hazard zone where the dazzle level ϵ is lower than that specific value: $E < \epsilon$. This means that the size of the dazzle spot in the camera image may decrease within the laser hazard zone (for the specific dazzle level E) as the imaging system approaches the laser source. For more details, see Ref. 8.
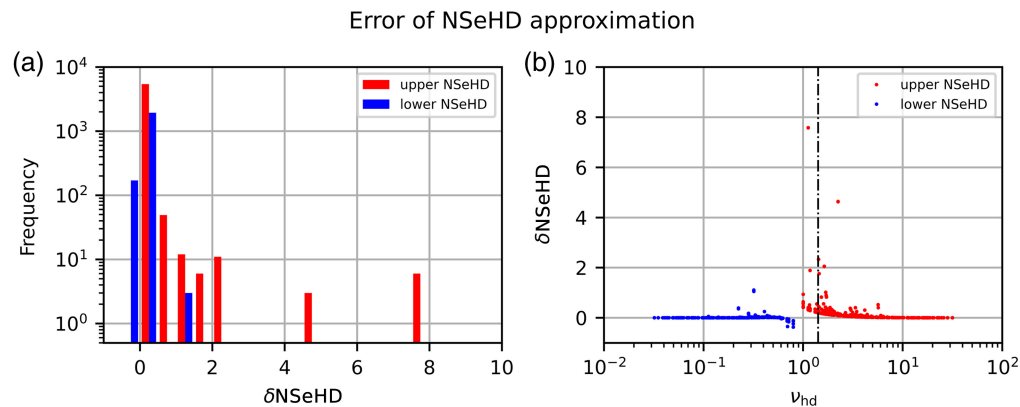
Fig. 6 Relative error δNSeHD according to Eq. (41) regarding the approximate NSeHD calculations. The red and blue data points correspond to the upper and lower values of the hazard distance, respectively. (a) Histogram showing the frequency of the δNSeHD values. (b) δNSeHD as a function of the numerically estimated truncation factor ν_{hd}. Image reproduced with permission from Ref. 8.

Due to this complexity, we decided to state only an approximation for the upper limit of the laser hazard zone in case of laser dazzle. Even for this limited case, we could not find a generally applicable approximation in a closed form. Nevertheless, we can give approximations for the NSeDD for two special cases: (a) For extended laser beams, i.e., the laser beam diameter is much larger than the aperture of the camera lens ($\nu \geq \sqrt{2}$). (b) For beam diameters that are smaller than the lens aperture ($\nu < \sqrt{2}$) in combination with larger dazzle levels. However, to anticipate, the accuracy of these approximations is not as good as in the case of the NSeHD.

The NSeDD in the case of extended laser beams ($\nu \geq \sqrt{2}$) can be approximately calculated by

$$\nu_{hd}^2 = \frac{2P_0 T}{E_{sat}f^2}\left(\frac{\lambda F}{\pi^3 f \Theta_\epsilon^3} + N_{ss}b_0\left[1 + \left(\frac{\Theta_\epsilon}{l}\right)^2\right]^{\frac{s}{2}}\right) - 2. \tag{42}$$

For laser beams with a diameter smaller than the aperture of the camera lens ($\nu < \sqrt{2}$), the NSeDD can be approximated by

$$\nu_{hd}^2 = 2\left[\frac{N_{ss}b_0 P_0 T}{E_{sat}f^2}\left(\frac{\Theta_\epsilon}{l}\right)^s\right]^{\frac{2}{2+s}}. \tag{43}$$

For Eq. (43), the following constraints have to be fulfilled:

$$\text{Constraint 1:} \quad \epsilon \gg \frac{2fl}{N_{max}p} = \frac{l}{\frac{FOV}{2}}, \tag{44}$$

$$\text{Constraint 2:} \quad \epsilon \gg \sqrt[s+3]{\frac{\lambda F l^s}{\pi^3 f N_{ss} b_0}} \cdot \frac{2f}{N_{max}p}. \tag{45}$$

Both constraints imply that the dazzle level ϵ should be sufficiently large, particularly that the influence of the scatter component outweighs that of the diffraction component regarding the focal plane irradiance distribution.

Finally, the NSeDD can be calculated using Eq. (42) or (43) by

$$\text{NSeDD} = \frac{\sqrt{\nu_{hd}^2 d_{ap}^2 - d_0^2}}{\Phi} = \frac{\sqrt{\nu_{hd}^2 f^2/F^2 - d_0^2}}{\Phi}. \tag{46}$$

Equivalently to the NSeHD, we also investigated the accuracy of these approximations. The NSeDD was first estimated using the approximation of Eqs. (42) and (43). Since both equations give an approximation for the upper limit of the laser hazard zone, we chose the maximum of both values for further processing (NSeDD_appr). Second, the NSeDD was computed by numerically solving Eq. (36) (NSeDD_num). Subsequently, the relative error of NSeDD_appr was calculated as before for the NSeHD

$$\delta\text{NSeDD} = (\text{NSeDD}_{appr} - \text{NSeDD}_{num})/\text{NSeDD}_{num}. \tag{47}$$

These calculations were performed for 2,292,924 different parameter sets.

In Fig. 7, the results are plotted for the NSeDD. In these graphs, the red color corresponds to the approximation for $\nu \geq \sqrt{2}$ calculated using Eq. (42). The blue color corresponds to the approximation for $\nu < \sqrt{2}$ calculated using Eq. (43). In the case of the NSeDD, we see a similar distribution in the histogram but not as good as for the NSeHD. Larger relative errors occur for the approximation for $\nu \geq \sqrt{2}$. We can recognize in the graph on the right-hand side that these cases mainly occur for values of the truncation factor $\nu_{hd} \approx \sqrt{2}$ but not exclusively. Furthermore, we can see that the relative error is negative for a considerable amount of the calculations. A negative relative error corresponds to an underestimation of the hazard distance. We conclude that Eqs. (42) and (43) have to be used with care for the estimation of hazard distances for sensor dazzle.

Error of NSeDD approximation
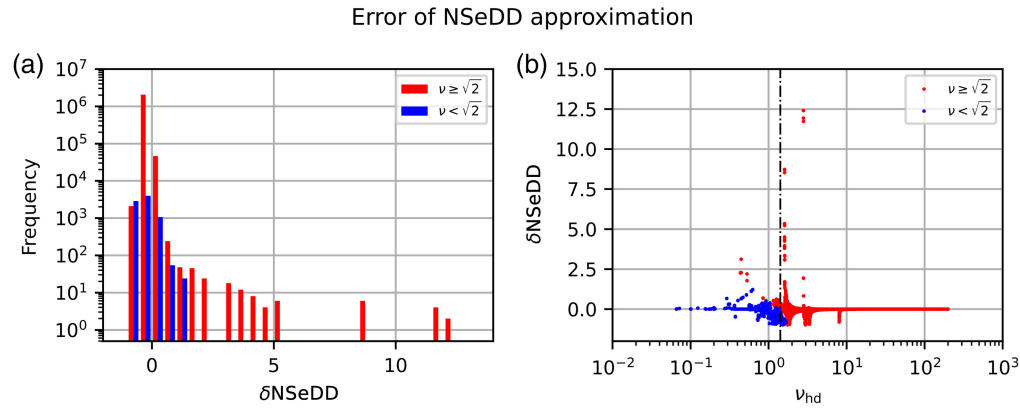
Fig. 7 Relative error δNSeDD according to Eq. (47) regarding the approximate NSeDD calculations. The red and blue data points correspond to the approximations for large and low values of the truncation factor ($\nu \geq \sqrt{2}$ and $\nu < \sqrt{2}$), respectively. (a) Histogram showing the frequency of the δNSeDD values. (b) δNSeDD as a function of the numerically estimated truncation factor ν_{hd}. Image reproduced with permission from Ref. 8.

7 Nonstandard Parameters for Laser Safety Calculations

7.1 Damage Thresholds of Image Sensors

Information on LIDTs of image sensors for continuous wave (cw) laser radiation in the visible spectral range is rare. Publications related to measured cw LIDT of CCD and CMOS cameras are, for example, Becker et al.,[13,14] Théberge et al.,[15] Burgess et al.,[16] Westgate and James[17] and Schwarz et al.[18–20] Here, we refer to a publication by Schwarz et al.[18] and summarize these threshold values in Table 3. Please note that Schwarz et al. measured these values for specific image sensors (CCD sensor: Sony ICX098, CMOS sensor: Aptina MT9V024). Laser damage thresholds for other types of image sensors may vary, but the order of magnitude ($10 - 100$ kW/cm^2) should be similar.

7.2 Saturation Thresholds of Image Sensors

The saturation threshold of an image sensor may be calculated using its technical specifications. At a specific irradiance $E_{sat,pixel}$ (i.e., the saturation irradiance), the number of photoelectrons μ_e generated by the incident photons within the camera's exposure time t_{exp} will equal the saturation capacity C of a pixel. Using this relation, the saturation irradiance of a pixel of size p can then be estimated by

$$E_{sat,pixel} = \frac{C \cdot hc/\lambda}{\eta A t_{exp}}. \tag{48}$$

Table 3 One-on-one LIDT measured for specific image sensors (CCD: Sony ICX098, CMOS: Aptina MT9V024). Data reproduced with permission from Ref. 18.

	One-on-one LIDT (kW/cm^2)			
	Exposure time (s)			
Image sensor	0.25	1	5	10
CMOS, monochrome	75 ± 7	73 ± 15	56 ± 4	48 ± 3
CMOS, color	56.7 ± 1.8	—	—	—
CCD, monochrome	146 ± 9	118 ± 9	93 ± 19	95 ± 21
CCD, color	14 ± 2	13 ± 2	11 ± 1	8.1 ± 0.8

Putting just the pixel saturation irradiance $E_{\text{sat,pixel}}$ from Eq. (48) into the MDE_S equations [Eqs. (24)–(27)] would imply that the image sensor is illuminated by the dazzle laser only. In a real situation, the imaging system typically observes a scene, which means that the charge generated by a pixel is determined by the ambient light of the scene and the laser light. To meet this condition, we assume that the operator or the camera's automatic exposure control will set the exposure time to a level, such that the image sensor's mean pixel signal equals roughly half of the maximum pixel signal. Thus, applying a factor of 0.5 to Eq. (48), we obtain a first estimate for the saturation irradiance E_{sat}

$$E_{\text{sat}} \approx 0.5 \cdot E_{\text{sat,pixel}} = 0.5 \cdot \frac{C \cdot \frac{hc}{\lambda}}{\eta A t_{\text{exp}}}. \tag{49}$$

If the saturation level sl of a camera image is known in more detail, e.g., when using a specific test chart in a laboratory environment, the saturation threshold may be estimated more precisely by

$$E_{\text{sat}} \approx (1 - sl) \cdot E_{\text{sat,pixel}} = (1 - sl) \cdot \frac{C \cdot hc/\lambda}{\eta A t_{\text{exp}}} \quad \text{with } sl \in [0, 1], \tag{50}$$

where a saturation level $sl = 0$ means not saturated and $sl = 1$ means completely saturated.

7.3 Scatter Parameters

In our simple theoretical model in Sec. 3, the scatter component E_{s} contributing to the focal plane irradiance distribution E_{fp} depends on the scatter parameters s/bb_0 and l of the camera lens used. Unfortunately, these scatter parameters are usually not known for commercial off-the-shelf (COTS) camera lenses. Thus, we performed a series of measurements where we recorded images of the focal plane irradiance distribution for a selection of seven typical camera lenses with focal lengths ranging from 25 to 100 mm. We then derived radial irradiance profiles from the image data and subsequently fitted our Eq. (4) to these irradiance profiles, where we used the quantities s/bb_0 and l as fit parameters. The outcome of this work was an individual set of scatter parameters for each camera lens under test; see Table 4. Since these sets describe the corresponding camera lens as a whole (and not the scattering properties of the single scattering surfaces), we denote them as *integrated scatter parameters*. Details can be found in Ref. 10.

We noticed that the integrated scatter parameters for the different camera lenses are of the same order of magnitude. Therefore, we additionally derived a generic set of integrated scatter parameters based on a statistical analysis of the individual sets. This generic set may be applied together with our equations to predict the laser dazzle of an electro-optical imaging system when a camera lens with unknown scatter parameters is used:

$$S = -1.86; \quad B = 0.36 \text{ sr}^{-1}; \quad B_0 = 6.92 \text{ sr}^{-1}; \quad L = 2.04 \text{ mrad}. \tag{51}$$

Table 4 Integrated scatter parameters for various commercial off-the-shelf camera lenses. Data reproduced with permission from Ref. 10.

Camera lens	s	b (sr^{-1})	b_0 (sr^{-1})	l (mrad)
Edmund Optics 54690	−2.24	0.36	8.96	2.39
Edmund Optics 67715	−1.79	0.48	1.23	5.75
Edmund Optics 86410	−2.23	0.32	12.85	1.99
LINOS MeVis-C 1.8-50	−1.83	0.33	6.74	2.02
Navitar NMV-75	−1.85	0.40	4.93	1.93
Navitar NMV-100	−1.90	0.37	18.01	1.31
Schneider Kreuznach Xenoplan 2.8/50	−1.88	0.41	2.76	3.95

8 Validation

The approximate equations for $\text{MPE}_S/\text{MDE}_S$ and NSeHD/NSeDD presented above only apply under the condition that the underlying theory of Sec. 3 is appropriate. To some extent, the equations were validated by our work published in Ref. 10, where we measured the integrated scatter parameters for various camera lenses; see Sec. 7.3. In this publication, we showed that the radial irradiance profile caused by incident laser irradiation can be described by our theoretical model. Nevertheless, it was our endeavor to test their usability following different approaches.

The first test (Sec. 8.1) was focused on the usability of the integrated scatter parameters as measured according to Ref. 10. Our theoretical model contains a couple of simplifications and assumptions, which may cast doubt on its suitability. Thus, we compared calculations of the focal plane irradiance distribution based on our theoretical model with the outcome of the optics design software FRED;[27] for a two-element lens and a lens of Double-Gauss type.

The second test (Sec. 8.2) was to compare the size of laser dazzle spots in camera images acquired during a field trial with the theoretical predictions of the dazzle spot size according to Eq. (33).

8.1 Validation Using the Optical Design Software FRED

The focal plane irradiance distribution was simulated for two different optical systems using the FRED optical design software from Photon Engineering:

1. a two-element laser focusing optics (LINOS 033486)
2. a generic camera lens of Double-Gauss type.

The advantage of using the two-element laser focusing optics was its availability and the disclosed optical design. This allowed us to measure (a) the integrated scatter parameters of the optics as well as (b) its modeling using the FRED software. We then compared the FRED simulation results (based on the measured integrated scatter parameters) with the outcome of our theoretical model to show that the theoretical model is reliable.

The FRED simulation results shall also serve to validate that our theoretical model, in conjunction with our generic set of integrated scatter parameters (see Sec. 7.3), is able to describe even quite complex multielement camera lenses as well. Hence, we simulated the irradiance distribution at the focal plane of the generic Double-Gauss camera lens using our generic set of scatter parameters; see Eq. (51). The design data of the Double-Gauss camera lens were taken from a standard textbook on optical design.[28]

The computation of the focal plane irradiance distribution using the FRED software was implemented by means of a multistep simulation. One simulation was focused on the diffraction component and the second one on the stray light component. The output of both simulation runs was then combined and subsequently compared with calculations based on Eq. (4); for details, see Ref. 11. Some results are presented in Fig. 8.

The scatter plots of Fig. 8 show the radial irradiance distribution as computed by the FRED software for the aforementioned optical systems and different values of the f-number F. Each data point corresponds to a simulated sensor pixel. The green data points correspond to the results of the simulation run focused on the scatter component, while the blue data points represent the result of the simulation run focused on the diffraction component. Their combination is plotted by red data points. Furthermore, the output of the theoretical model is plotted as a black solid curve. For the LINOS 033486 laser focusing lens [Figs. 8(a) and 8(b)], we can see that the theoretical model predicts quite well the envelope of the FRED-simulation data. Of course, obtaining such a good result for this focusing lens is not really surprising since it has a rather simple optical design, and the integrated scatter parameters have been experimentally determined and served as an input for the FRED simulation.

Regarding the Double-Gauss camera lens [Figs. 8(c) and 8(d)], one may recognize for radial coordinates <10 pixels that there is a larger deviation between the results of the model and the simulations, which we attribute to aberrations that are not covered by our theoretical model. For radial coordinates larger than ∼10 pixels, we can see from the scatter plots that the theoretical model fits reasonably to the simulation results. For small f-numbers, see Fig. 8(c), there seems to be an overestimation of the irradiance, while for large f-numbers, see Fig. 8(d), an
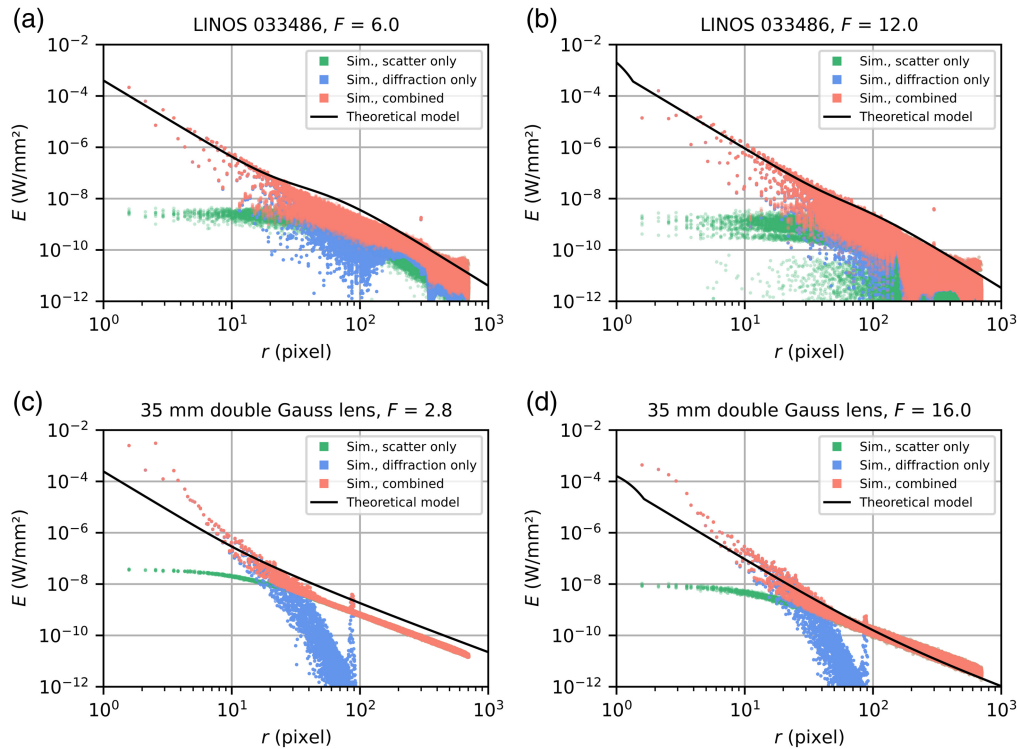
Fig. 8 Comparison of the simulation results using the FRED optical design software (colored points) with the theoretical model according to Eq. (4) (black curve). (a) LINOS 033486, $F = 6.0$; (b) LINOS 033486, $F = 12.0$; (c) generic Double-Gauss lens, $F = 2.8$; and (d) generic Double-Gauss lens, $F = 16.0$. Graphs reproduced with permission from Ref. 11.

underestimation occurs. Nevertheless, we got an adequate agreement between our simplified theoretical model and the output of the corresponding FRED simulation.

8.2 Validation Using Data from Outdoor Measurements

During a field trial, an electro-optical imaging system at a distance of 660 m was dazzled on a slant path by cw laser radiation.[29] Camera images were acquired for various laser wavelengths and camera exposure times. In the subsequent data analysis, dazzle spot sizes were assessed using overexposed pixel counting (OPC) and then compared to the theoretical predictions of the dazzle spot size according to Eq. (33).

As dazzler, we used the Toptica iChrome MLE multiwavelength laser device. This laser source comprises four different lasers (wavelengths 488, 515, 561, and 640 nm) with output powers ranging from 40 to 100 mW. The data of the laser device are listed in Table 5. The actually used laser output power P_0 was measured during the field trial, whereas the output diameter d_0 and full angle divergence Φ were measured in the laboratory using an M^2 measurement system (Thorlabs M2MS-BC106VIS/M). The laser beam diameter d_{86} at the imaging system was calculated from these data using Eq. (2). For the atmospheric attenuation of the laser radiation, we assumed an extinction coefficient of $\mu = 0.2$ km^{-1} since the weather conditions were good.

The imaging system consisted of a Schneider-Kreuznach Xenoplan 2.8/50 COTS camera lens[30] mounted to an Allied Vision Mako G-223B NIR camera.[31] The specifications of both devices are also listed in Table 5. The transmittance T of the camera lens was not known. Thus, we assumed a broadband antireflection coating with a reflection below <0.5% per surface, resulting in $T = (1 - 0.005)^{2 \cdot N_{oe}} = 0.94$. Furthermore, we intentionally did not measure the scatter parameters of this camera lens but simply used the generic set of integrated scatter parameters as stated in Eq. (51) to investigate their applicability. The data of the camera were taken from the datasheet, see Ref. 31. From the corresponding graph of the data sheet, we estimated a quantum efficiency of $\eta \approx 0.7$ for the laser wavelengths used.

Table 5 Device parameters used for the evaluation of the measurement data gained during the field trial.

Laser				
Wavelength λ	488 nm	515 nm	561 nm	640 nm
Output power P_0	89.6 mW	37.2 mW	89.5 mW	48.4 mW
Output diameter d_0	0.85 mm	0.94 mm	0.96 mm	1.11 mm
Full angle divergence $(1/e^2)$ Φ	0.89 mrad	0.86 mrad	0.89 mrad	0.84 mrad
Camera lens				
Focal length f		50 mm		
f-Number F		2.8		
No. of optical elements N_{oe}		6		
Transmittance T		0.94 (assumed)		
Scatter parameter (@ 550 nm) s		-1.86 (assumed)		
Scatter parameter (@ 550 nm) b		0.36 sr^{-1} (assumed)		
Scatter parameter (@ 550 nm) l		2.04 mrad (assumed)		
Image sensor/camera				
Size $(N_{col}\times)$ N_{row}		2048 px. $\times$ 1024 px.		
Pixel size p		5.5 μm		
Quantum efficiency η		$\sim$0.7		
Exposure time t_{exp}		100 μs/1 ms/10 ms		
Saturation capacity C		9300 e$^-$		
Miscellaneous				
Atmospheric extinction coefficient μ		0.2 km^{-1}		

In summary, our set of measured, specified, and estimated values represents a quite suitable mix for testing the usability of our approach.

In Fig. 9, some examples of camera images are shown for the laser wavelengths of 515 and 640 nm. The images were taken using three different exposure times of 100 μs, 1 ms, and 10 ms. The data was processed according to the following way:

1. Calculation of a mean image: For each parameter setting (combination of laser wavelength and camera exposure time), a mean image from 20 consecutive frames of the video stream was calculated.

2. OPC: The number of overexposed pixels in each mean image was counted. Using this number, the nominal size of the dazzle spot could be estimated for each mean image. We denote this quantity as *nominal size* since the method assumes a circular dazzle spot, which of course is not exactly true, particularly for measurements affected by the atmosphere.

3. Estimation of the dazzle spot size using a saturation level of $sl = 0.5$: The dazzle spot size according to our theoretical model was calculated using Eq. (33) by applying the parameters of Table 5 and estimating the saturation threshold according to Eq. (49), i.e., the saturation level of the whole image was assumed to be $sl = 0.5$.

4. Estimation of the dazzle spot size using an image-specific saturation level (ISSL): The dazzle spot size according to our theoretical model was calculated using Eq. (33) by applying the parameters in Table 5 and estimating the saturation threshold according to Eq. (50).
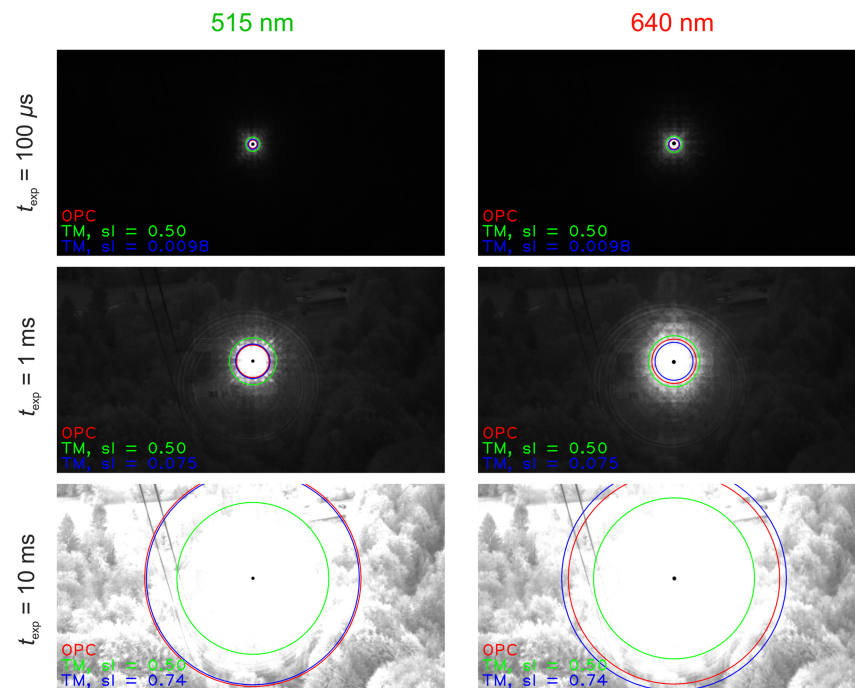
Fig. 9 Dazzling of an electro-optical imaging system by laser radiation of the wavelength 515 and 640 nm. The images were acquired during an outdoor field trial on a slant path. Dazzle spot sizes computed by OPC are indicated by red circles. Furthermore, dazzle spot sizes as calculated by Eq. (33) using saturation levels of 0.5 (green circles) or image-specific saturation levels (blue circles) are shown.

In this case, the saturation level sl was determined from the mean images. For this, the mean value of strips of pixels at the left and right border of the mean images (width every 200 pixels) was divided by the maximum possible pixel value to estimate roughly the saturation level sl.

The three calculated dazzle spot sizes are drawn into the camera images of Fig. 9 as colored circles. Red circles indicate the dazzle spot size as calculated by the OPC method. The dazzle spot sizes according to our theoretical model are drawn as green and blue circles for a saturation level of 0.5 and the image-specific saturation level, respectively.

Looking at Fig. 9, we can see that our approach for laser safety calculations can indeed give a reasonable estimate for the dazzle spot sizes. In the case of the underexposed images ($t_{\exp} = 100$ ms and $t_{\exp} = 1$ ms), the use of ISSL leads to a very good agreement between the OPC result and the calculated dazzle spot size using the theoretical model. Using the saturation level $sl = 0.5$ slightly overestimates the dazzle effect but not to an extraordinary degree.

In the case of the slightly overexposed images ($t_{\exp} = 10$ ms), the theoretical prediction of the dazzle spot size for saturation level 0.5 fits quite well to the dazzled area of the camera image, whereas there is an overestimation using the image-specific saturation level. At first glance, one might say that the calculated dazzle spot size using the ISSL fits quite well with the dazzle spot size computed using the OPC method. However, one has to keep in mind that the camera image was slightly overexposed, which means that the OPC method also counts pixels overexposed by ambient light and not only by laser light. Thus, the dazzle spot size computed with the OPC method overestimates the laser effect.

The results for all laser wavelengths used at the field trial and for all values of camera exposure time are presented in the graphs of Fig. 10. For each laser wavelength, there is a graph that contains the results of the calculations according to the theoretical model and the OPC evaluation applied to the image data. The theoretical results comprise both the use of saturation level $sl = 0.5$ and the ISSL. The graphs also confirm the above statements for the other laser wavelengths of 488 and 561 nm.

Comparison of theoretically and experimentally determinded dazzle spot sizes
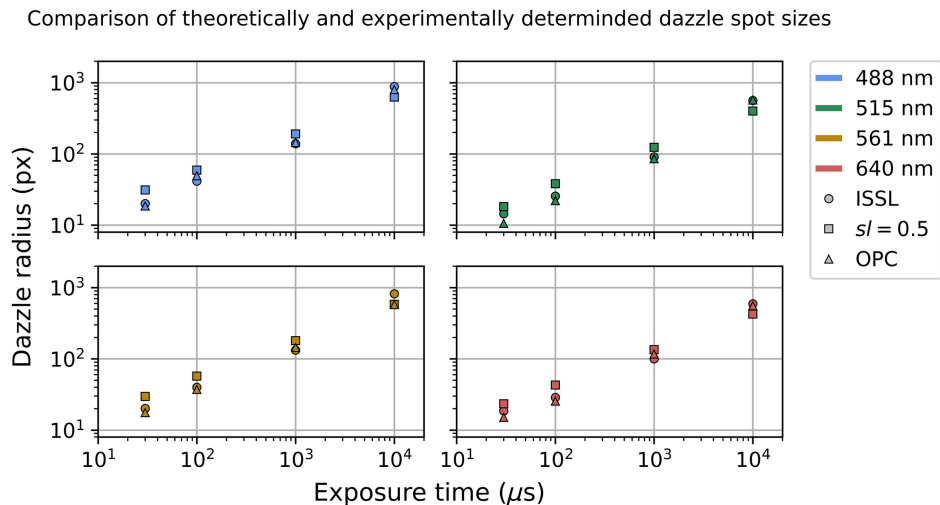
Fig. 10 Comparison of theoretically and experimentally determined dazzle spot sizes for different laser wavelengths. Abbreviations: ISSL, image-specific saturation level; sl, saturation level; OPC, overexposed pixel counting.

In summary, there is a good agreement between theory and experiment, considering that not all parameters involved were exactly specified. Since the underlying theory for the prediction of dazzle spot sizes is the same as for the estimation of the ELs MPE_S and MDE_S, we assume that the equations for estimating the ELs can also be considered validated.

9 Conclusions

In this publication, we presented an approach for laser safety calculations for electro-optical imaging systems. It includes a set of equations to estimate ELs and hazard distances regarding laser-induced damage and dazzle. Furthermore, dazzle spot sizes can be predicted. All equations are in closed form, which allows their use, in principle, with a pocket calculator, a pen, and a sheet of paper. A computer is not necessary to numerically solve equations, even though we have to admit that some of the equations are somewhat longer and a computer may still be helpful.

Furthermore, we tried to include in our equations only standard parameters of the involved systems (laser, camera lens, image sensor) that are typically specified by the manufacturer. However, some nonstandard parameters have to be known, which are: the LIDT and saturation threshold of the image sensor as well as the (integrated) scatter parameters of the camera lens. Values for LIDTs of image sensors can be found in the literature; saturation thresholds can be calculated from the image sensor's specifications. Regarding scatter parameters for commercial off-the-shelf camera lenses, we performed a series of experiments to measure them. From these measurements, we derived a generic set of scatter parameters that may be used if the exact values for specific camera lenses are not available.

To validate our theory, i.e., the derived closed-form equations as well as the generic set of scatter parameters, we performed several experimental tests, field trials, and optics modeling. In our opinion, our studies indicate the suitability of our equations for the desired application: laser safety calculations for electro-optical imaging systems.

Disclosures

The authors have no relevant financial interests in the study and no other potential conflicts of interest.

Code and Data Availability

The data that support the findings of this article are not publicly available due to classification. They can be requested from the author at gunnar.ritt@iosb.fraunhofer.de.

References

1. American National Standard, "Safe use of lasers outdoors," ANSI Z136.6-2015, Laser Institute of America, Orlando, FL, USA (2015).
2. Bundesanstalt für Arbeitsschutz und Arbeitsmedizin (BAuA), "TROS Laserstrahlung Teil 2: Messungen und Berechnungen von Expositionen gegenüber Laserstrahlung," (2018).
3. American National Standard, "Safe use of lasers," ANSI Z136.1-2022, Laser Institute of America, Orlando, FL, USA (2022).
4. European Standard, "Personal eye-protection equipment—filters and eye-protectors against laser radiation (laser eye-protectors)," EN 207:2017 (2017).
5. C. A. Williamson and L. N. McLin, "Nominal ocular dazzle distance (NODD)," *Appl. Opt.* **54**, 1564–1572 (2015).
6. C. A. Williamson and L. N. McLin, "Determination of a laser eye dazzle safety framework," *J. Laser Appl.* **30**, 032010 (2018).
7. C. A. Williamson and L. N. McLin, "Laser eye dazzle safety framework," in *Int. Laser Saf. Conf.*, pp. 164–165 (2017).
8. G. Ritt, "Laser safety—what is the laser hazard distance for an electro-optical imaging system?" *Sensors* **23**, 7033 (2023).
9. G. Ritt, "Laser safety calculations for imaging sensors," *Sensors* **19**, 3765 (2019).
10. G. Ritt, B. Schwarz, and B. Eberle, "Estimation of lens stray light with regard to the incapacitation of imaging sensors," *Sensors* **20**, 6308 (2020).
11. B. Schwarz, G. Ritt, and B. Eberle, "Estimation of lens stray light with regard to the incapacitation of imaging sensors—part 2: validation," *Sensors* **22**, 9447 (2022).
12. G. Ritt et al., "An approach for laser safety calculations for electro-optical imaging systems," *Proc. SPIE* **12738**, 127380F (2023).
13. M. F. Becker et al., "Laser-induced damage to silicon CCD imaging sensors," *Proc. SPIE* **1105**, 68–77 (1989).
14. M. F. Becker et al., "Laser-induced functional damage to silicon CCD sensor arrays," *Proc. SPIE* **1624**, 67–79 (1992).
15. F. Théberge et al., "Damage thresholds of silicon-based cameras for in-band and out-of-band laser expositions," *Appl. Opt.* **61**, 2473–2482 (2022).
16. C. Burgess et al., "Modelled and experimental laser-induced sensor damage thresholds to continuous wave infrared sources," *Proc. SPIE* **10797**, 107970T (2018).
17. C. Westgate and D. James, "Visible-band nanosecond pulsed laser damage thresholds of silicon 2D imaging arrays," *Sensors* **22**, 2526 (2022).
18. B. Schwarz et al., "Laser-induced damage threshold of camera sensors and micro-optoelectromechanical systems," *Opt. Eng.* **56**, 034108 (2017).
19. B. Schwarz et al., "Further investigation on laser-induced damage thresholds of camera sensors and micro-optomechanical systems," *Proc. SPIE* **11161**, 111610A (2019).
20. B. Schwarz, G. Ritt, and B. Eberle, "Impact of threshold assessment methods in laser-induced damage measurements using the examples of CCD, CMOS, and DMD," *Appl. Opt.* **60**, F39–F49 (2021).
21. K. W. Benoist and R. (H.) M. A. Schleijpen, "Modelling of the over-exposed pixel area of CCD cameras caused by laser dazzling," *Proc. SPIE* **9251**, 92510H (2014).
22. G. L. Peterson, "Analytic expressions for in-field scattered light distributions," *Proc. SPIE* **5178**, 184–193 (2004).
23. E. C. Fest, *Stray Light Analysis and Control*, SPIE Press, Bellingham, Washington, USA (2013).
24. Breault Research Organization, Inc., "Scattering in ASAP," http://www.breault.com/knowledge-base/scattering-asap (accessed 18 May 2020).
25. S. J. Wein, "Small-angle scatter measurement," PhD Thesis, The University of Arizona, Tucson, AZ, USA (1989).
26. H. Urey, "Spot size, depth-of-focus, and diffraction ring intensity formulas for truncated Gaussian beams," *Appl. Opt.* **43**, 620–625 (2004).
27. FRED Software, "Photon engineering," https://photonengr.com/fred-software/ (accessed 19 July 2023).
28. M. Laikin, *Lens Design*, Chap. 6, 4th ed., CRC Press, Boca Raton, FL, USA (2007).
29. B. Eberle et al., "NATO SET-249 joint measurement campaign on laser dazzle effects in airborne scenarios," *Proc. SPIE* **11161**, 111610C (2019).
30. Jos. Schneider Optische Werke GmbH, "Datasheet Schneider-Kreuznach Tourmaline 2.8/50 (formerly Schneider-Kreuznach Xenoplan 2.8/50)," https://schneiderkreuznach.com/application/files/6216/4241/8065/TOURMALINE_28_50_C_1001976_datasheet.pdf (accessed 20 July 2023).
31. Allied Vision Technologies GmbH, "Datasheet allied vision Mako G-223B NIR," https://cdn.alliedvision.com/fileadmin/pdf/de/Mako_G-223B_NIR_DataSheet_de.pdf (accessed 20 July 2023).

Gunnar Ritt is a research associate at Fraunhofer IOSB, Ettlingen, Germany. He received his diploma and PhD degrees in physics from the University of Tübingen, Germany, in 1999 and 2007, respectively. His main research focus is on laser protection.

Bastian Schwarz has been a research scientist at Fraunhofer IOSB, Ettlingen, Germany, since 2013 and has been the head of the optical countermeasure group since 2022. He graduated in physics from the University of Freiburg in 2012. Since 2013, his research areas include laser protection and laser damage performance.

Bernd Eberle has been a senior scientist at Fraunhofer IOSB in Ettlingen, Germany, where he headed the optical countermeasure and laser protection group. He received his diploma and PhD degrees in physics from the University of Konstanz in 1983 and 1987, respectively. His research activities included laser technology, laser spectroscopy, nonlinear optics, femtosecond optics, optical countermeasures, including protection against laser radiation, and imaging laser sensors.

Michael Henrichsen is a research associate at Fraunhofer IOSB, Ettlingen, Germany. He has been the head of the optronic analysis systems and laser effects group since 2022. He received his master of science degree in physics from the University of Constance, Germany, in 2012. His main research focus is on laser effects and infrared imaging.